Azimuthal Spoke Propagation in Hall Effect Thrusters

Michael J. Sekerak, Benjamin W. Longmier, Alec D. Gallimore, Daniel L. Brown, Richard R. Hofer, and James E. Polk

***Abstract*— Spokes are azimuthally propagating perturbations in the plasma discharge of Hall effect thrusters (HETs) that travel in the $E \times B$ direction. The mechanisms for spoke formation are unknown, but their presence has been associated with improved thruster performance in some thrusters motivating a detailed investigation. The propagation of azimuthal spokes are investigated in a 6 kW HET by using high-speed imaging and azimuthally spaced probes. The spoke velocity is determined from high-speed image analysis using three methods with similar results. The spoke velocity for three discharge voltages (300, 400, and 450 V) and three anode mass flow rates (14.7, 19.5, and 25.2 mg/s) are between 1500 and 2200 m/s across a range of magnetic field settings. The spoke velocity is inversely dependent on magnetic field strength for lower B-fields and asymptotes at higher B-fields. Spoke velocities calculated from the probes are consistently higher by 30% or more. An empirically approximated dispersion relation of $\omega^\alpha = v_{\text{ch}}^\alpha k_\theta^\alpha - \omega_{\text{ch}}^\alpha$ where $\alpha \geq 1$ yields a characteristic velocity that matches the ion acoustic speed for ∼5 eV electrons which exist in the near-anode and near-field plume regions of the discharge.**

***Index Terms*— Aerospace industry, hall effect devices, plasma diagnostics, plasma measurements, plasma waves, satellites, space technology.**

Manuscript received November 5, 2013; revised June 4, 2014; accepted September 1, 2014. This work was supported in part by a NASA Office of the Chief Technologist's Space Technology Research Fellowship, in part by the U.S. Air Force Office of Scientific Research, Arlington, VA, USA, and the Air Force Research Laboratory, Edwards AFB, CA, USA, through the Michigan/Air Force Center of Excellence in Electric Propulsion under Grant FA9550-09-1-0695, in part by ERC, Inc., Huntsville, AL, USA, under Contract RS130040 and Contract RS140086, and in part by the Jet Propulsion Laboratory, California Institute of Technology, Pasadena, CA, USA, within the National Aeronautics and Space Administration (NASA).

M. J. Sekerak, B. W. Longmier, and A. D. Gallimore are with the Plasmadynamics and Electric Propulsion Laboratory, Department of Aerospace Engineering, University of Michigan, Ann Arbor, MI 48109 USA (e-mail: msekerak@umich.edu; longmier@umich.edu; alec.gallimore@umich.edu).

D. L. Brown is with the U.S. Air Force Research Laboratory, Edwards AFB, CA 93524 USA (e-mail: daniel.brown@edwards.af.mil).

R. R. Hofer is with the Electric Propulsion Group, Jet Propulsion Laboratory, Pasadena, CA 91125 USA, managed by Californial Institute of Technology (e-mail: richard.r.hofer@jpl.nasa.gov).

J. E. Polk is with the Propulsion and Materials Engineering Section, Jet Propulsion Laboratory, Pasadena, CA 91109 USA, managed by California Institute of Technology, Pasadena (e-mail: james.e.polk@jpl.nasa.gov).

Color versions of one or more of the figures in this paper are available online at http://ieeexplore.ieee.org.

Digital Object Identifier 10.1109/TPS.2014.2355223

NOMENCLATURE

A_0	Amplitude for Lorentzian fit, arb. units Hz^{-1}.
B	Magnetic field, T.
B_r	Radial magnetic field, T.
B_r/B_r^*	Normalized radial magnetic field.
$b_{j,k}$	Bin j, k.
E_z	Axial electric field, V m^{-1}.
f	Frequency, Hz.
f_c	Camera frame rate, frames s^{-1}.
f_m	Peak frequency for spoke order m, Hz.
f_0	Center frequency for Lorentzian fit, Hz.
$I_{\text{IM,OM}}$	Inner, outer magnet coil current, A.
j_D	Discharge current density, mA cm^{-2}.
k_θ	Azimuthal wave number, rad m^{-1}.
L_{chnl}	Discharge channel length, m.
L_{pr}	Probe spacing, m.
m	Spoke order.
m_{min}	Minimum spoke order.
$m_{i,e}$	Ion, electron mass, kg.
N_{bins}	Number of bins.
N_{fr}	Number of frames.
n	Plasma density, m^{-3}.
PSD	Power spectral density, arb. units Hz^{-1}.
q	Elementary charge, C.
R_{chnl}	Mean discharge channel radius, m.
R_{jk}	Linear cross correlation between b_j and b_k.
r	Radial location, m.
T_e	Electron temperature, eV.
t_d	Probe time delay, s.
$t_{j,k}$	Time delay from bin j to k, s.
v_{ch}	Characteristic velocity, m s^{-1}.
v_{ci}	Critical ionization velocity, m s^{-1}.
$v_{E\times B}$	$E \times B$ drift velocity, m s^{-1}.
v_{gr}	Group velocity, m s^{-1}.
v_{ph}	Phase velocity, m s^{-1}.
v_s	Ion acoustic velocity, m s^{-1}.
v_{sp}	Spoke velocity, m s^{-1}.
$v_{\text{spj},k}$	Spoke velocity from bin j to k, m s^{-1}.
v_{th_e}	Electron thermal velocity, m s^{-1}.
v_θ	Azimuthal velocity, m s^{-1}.
w_m	Weighting for spoke order, m.
z	Axial location, m.
α	Dispersion relation power dependence.
β	Spoke velocity to B_r/B_r^* power dependence.

Γ	Full-width at half maximum for Lorentzian fit, Hz.
η	Plasma resistivity, Ω m.
$\eta_\perp$	Cross-field plasma resistivity, Ω m.
$\Delta\theta_{j,k}$	Angular difference from bin j to k, deg.
$\dot{\theta}_{\mathrm{sp}}$	Spoke angular velocity, deg s^{-1}.
ν_{ef}	effective collision frequency, s^{-1}.
τ_s	shutter period, s.
Ω_e	electron Hall parameter, rad s^{-1}.
ω	frequency, rad s^{-1}.
ω_{ch}	characteristic frequency, rad s^{-1}.
$\omega_{\mathrm{ci},e}$	ion, electron cyclotron frequency, rad s^{-1}.

I. Introduction

SPOKES were first observed in Hall effect thruster (HET)-type devices by Janes and Lowder [1] as a possible mechanism for cross-field transport. Research on a cylindrical Hall thruster (CHT) [2], [3] showed that up to half of the discharge current can pass through a spoke. It was also reported that the CHT performance (measured by discharge current) increased when the spoke was not present [4]. This can lead one to conclude that spokes are detrimental to HET performance. However, the annular device studied by Janes and Lowder differed from modern HETs and the CHT has a significantly different magnetic field topology and physical geometry (no inner wall); so direct comparisons may not be appropriate with those systems to modern annular HETs such as the SPT-100 and H6.

Research by Brown and Gallimore [5] and McDonald and Gallimore [6] on low-voltage operation showed that thruster performance increased when spokes were stronger in the H6. Recent results by Sekerak *et al.* [7] on mode transitions clearly shows that spoke behavior was dominant in so-called local oscillation mode where the thruster exhibited lower mean discharge current and discharge current oscillation amplitude. The H6 thrust-to-power is maximum when the thruster is operating in local mode with spokes clearly propagating and no significant breathing mode. Sekerak *et al.* [7] raise the causality question of whether spokes are responsible for the improved thruster performance or are indicators that the thruster is running optimally. Regardless, the association of spokes with improved thruster performance in the H6 warrants an in-depth interrogation of the fundamental mechanism(s) that drive them in HETs.

This paper is organized as follows. Section II reviews the experimental setup and findings of the recent investigation into mode transitions that were intentionally induced by varying magnetic field. Section III describes different methods for calculating azimuthal spoke velocity. Section IV discusses the results of four different methods used to calculate spoke velocity with the correlation method as the preferred technique. Across a range of normalized magnetic field settings, the spoke velocity is 1500–2200 m/s for all operating conditions. An empirically approximated dispersion relation of $\omega^\alpha = v_{\mathrm{ch}}^\alpha k_\theta^\alpha - \omega_{\mathrm{ch}}^\alpha$ where $\alpha \geq 1$ yields a characteristic velocity that matches the ion acoustic speed for ~5 eV electrons, which have been measured in the near-anode and near-field plume regions of the discharge channel. Finally, observations of spoke characteristics are summarized to guide theory development.

II. Review of Mode Transition Oscillations

This section reviews a recent investigation into mode transitions in HETs that were intentionally induced by varying magnetic field strength [7]. The high-speed imaging results and probe data from this experiment are used in Section III to develop methods for calculating azimuthal spoke velocity and determine how spoke velocity varies with magnetic field strength.

HETs have been under development for over 50 years with significant experimental and flight histories [8] and mode transitions have been commonly observed throughout their development as noted by some of the early pioneering Russian research [9]. HETs have several parameters that define a single operating point such as discharge voltage, magnetic field strength (or magnet coil current), anode mass flow rate, and cathode mass flow rate. Laboratory HET discharge power supplies operate in voltage-regulated mode where the discharge voltage between the anode and cathode is held constant and the discharge current is allowed to fluctuate. A general, qualitative description of mode transition can be deduced from previous research as the point at which, while varying one parameter and maintaining all others constant, a sharp discontinuity is observed in the mean discharge current and oscillation amplitude. In one mode, the discharge current oscillation amplitude is small with respect to the mean discharge current value, whereas after the mode transition the mean discharge current rises sharply as well as the oscillation amplitude. Previous researchers have identified mode transitions in HETs [5], [9], [10] where a small change in a thruster operating parameter such as discharge voltage, magnetic field or mass flow rates causes the thruster mean discharge current and oscillation amplitude to increase significantly and decrease thruster performance [7]. Thrust-to-power is maximized in the mode where azimuthal spokes are present and begins to decrease by up to 25% when absent. Although spokes are not identified as the cause of the increased performance, their association suggests that investigating the underlying mechanism of spokes will benefit thruster operation.

A. Thruster and Facilities

A recent experiment induced mode transitions in a 6 kW class laboratory HET called the H6 shown in Fig. 1. The experimental setup is described in detail in [7] and only pertinent details are repeated here. The investigation was conducted in the large vacuum test facility (LVTF) of the Plasmadynamics and Electric Propulsion Laboratory (PEPL) at the University of Michigan, MI. The test matrix included variations in discharge voltage and xenon propellant flow rates. Propellant mass flow rates tested were 25.2, 19.5, and 14.7 mg/s through the anode and 1.8, 1.4, and 1.0 mg/s (7% cathode flow fraction) through the LaB_6 cathode. Discharge voltages of 300, 400, and 450 V were applied between the anode and cathode. The xenon-corrected chamber pressures were 8.5×10^{-6}, 1.1×10^{-5}, and 1.4×10^{-5} torr for

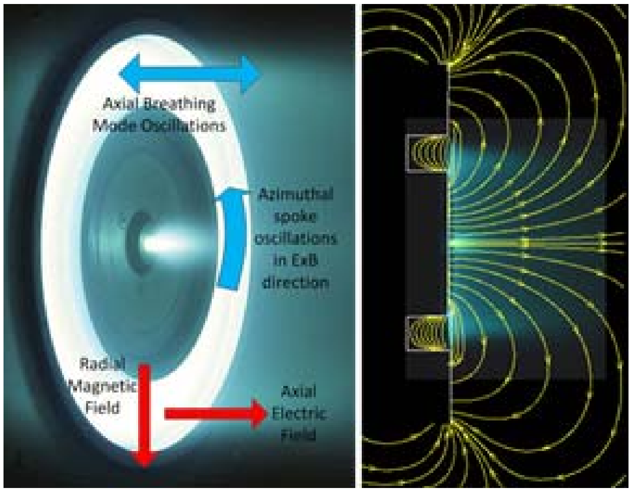

Fig. 1. Left: H6 with direction of magnetic field and $E \times B$ shown. Right: profile picture of the H6 operating at nominal conditions with magnetic field stream lines overlaid and discharge channel outlined. Reproduced from [7, Fig. 6].

14.7, 19.5, and 25.2 mg/s anode flow rate, respectively. These pressures were measured with an external ionization gauge and differ from the previously reported pressures [7] that were measured with a nude ionization gauge. Both of these gauges are mounted at the top of LVTF above the thruster (~3 m away) and the pressure measurement uncertainty was estimated to be 20% [11]. A more complete discussion of pressure measurements and pressure effects on HET operation is provided by Walker [12].

The H6 was a joint development effort of the University of Michigan, the Air Force Research Laboratory (AFRL) at Edwards AFB, and the NASA Jet Propulsion Laboratory (JPL); a separate copy of the thruster is maintained at each institution. It is notable for its high total efficiency; for example, 64% at 300 V (6 kW) with a specific impulse of 1950 s and 70% at 800 V (6 kW) with a specific impulse of 3170 s [13]. Since first firing in 2006, the H6 has been well-characterized by a variety of diagnostic and modeling techniques at Michigan, AFRL, and JPL. The magnetic field shape shown in Fig. 1 was kept constant during testing, though the magnitude, noted by B_r/B_r^*, was varied throughout the testing to induce a mode change within the H6.[1]

The quantity B_r/B_r^* is the maximum radial magnetic field value at a particular setting of inner magnet (I_{IM}) current and outer magnet (I_{OM}) current divided by the reference maximum radial magnetic field. The reference magnetic field (B_r^*) strength at 300 V and 20 A discharge current is $I_{\text{IM}} = 3.50$ A and $I_{\text{OM}} = 3.13$ A [13]. To confirm magnetic field shape consistency, simulations were performed using MagNet Version 7.4.1.4 (32 b) from Infolytica Corporation for all magnet settings used during B-field sweeps. The maximum deviation in magnetic field direction on channel centerline $\pm L_{\text{chnl}}/4$ from the exit plane with respect to the reference magnetic field was less than 1° [14].

[1]References to magnetic field strength or magnitude in this paper are synonymous with magnetic flux density, and magnetic field shape or streamlines are synonymous with magnetic lines of force.

B. FastCam and ISR Probes

High-speed imaging was acquired with a Photron SA5 FastCam with a Nikon ED AF Nikkor 80–200 mm lens at its maximum aperture f/2.8. The SA5 is capable of up to 1 000 000 frames/s with 128 × 16 pixel resolution, but was used at 87 500 frames/s with 256 × 256 pixel resolution for this investigation. The camera was 6 m downstream from the thruster outside LVTF with a view of the thruster through a viewport. In Fig. 2, three monochromatic FastCam frames 45.7 μs apart have been enhanced with false-colors to emphasize the propagating spokes. FastCam frames are every 11.4 μs with the frame rate of 87.5 kHz, so there are two frames between each of the frames shown. The spoke can be seen to move approximately ~45° in ~45 μs, which corresponds to an approximate spoke velocity of ~1400 m/s.

Details of the McDonald technique for high-speed image analysis (HIA) are given in [7], [14], and [15], but a brief summary is provided here. The monochromatic video is imported into MathWorks MATLAB where each frame is a 256 × 256 matrix of light intensity values and the ac component is subtracted individually from each pixel. The discharge channel is isolated and divided into 180 two-degree bins. The pixels in each bin are averaged together generating a 180 × 1 vector of light intensity for each frame. A 2-D plot of all frames is the spoke surface where the ordinate is azimuthal location around the discharge channel in clock positions and the abscissa is time with each vertical column of values representing one frame of video. Adding all bins together yields the $m = 0$ or m_0 mode and was first shown by Lobbia *et al.* [16] to linearly correlate to the discharge current. During the mode transition investigation reported in [7] the same strong, linear correlation was also observed and used as the basis for converting light intensity to discharge current density with several assumptions.

The spoke surface or discharge current density surface yields valuable information on plasma oscillations within the discharge channel by showing the time-resolved, azimuthal distribution of light intensity. Vertical features represent extremes in discharge current density that occur everywhere in the channel simultaneously. Diagonal features are perturbations in discharge current density that propagate azimuthally around the discharge channel. Lines from upper-left to lower-right are propagating anticlockwise around the discharge channel and lines from the lower-left to upper-right are propagating clockwise. The $E \times B$ direction in the H6 is anticlockwise, because the B-field direction is radially out. It was shown that all azimuthally propagating features are in that direction represented by lines from upper-left to lower-right with the slope corresponding to propagation velocity in degree/s. The HIA and 2-D power spectral density (PSD) are discussed further in Section III-C.

Ion saturation reference (ISR) probes were positioned 1.5 discharge channel mean radii downstream at the 6 o'clock position on thruster center line as shown in [7, Fig. 9]. The ISR probe gap was 29.5 ± 0.5 mm apart, which corresponds to 21.4° ± 1.7° of azimuthal spacing, that is, ~11° on either side of 6 o'clock. The probes were 0.13 mm diameter pure tungsten wire with 3 mm exposed. The ISR probes were biased to

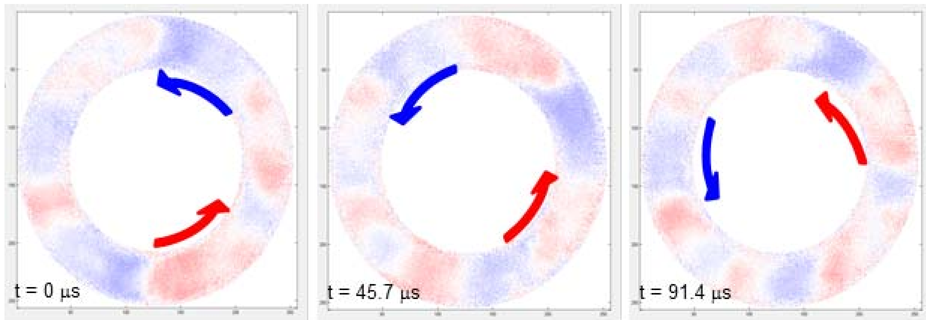

Fig. 2. Three false-colored FastCam frames 45.7 μs apart from a seven frame series showing azimuthal spoke propagation. Red: bright regions (spokes) of the discharge channel. Blue: dim regions of the discharge channel.

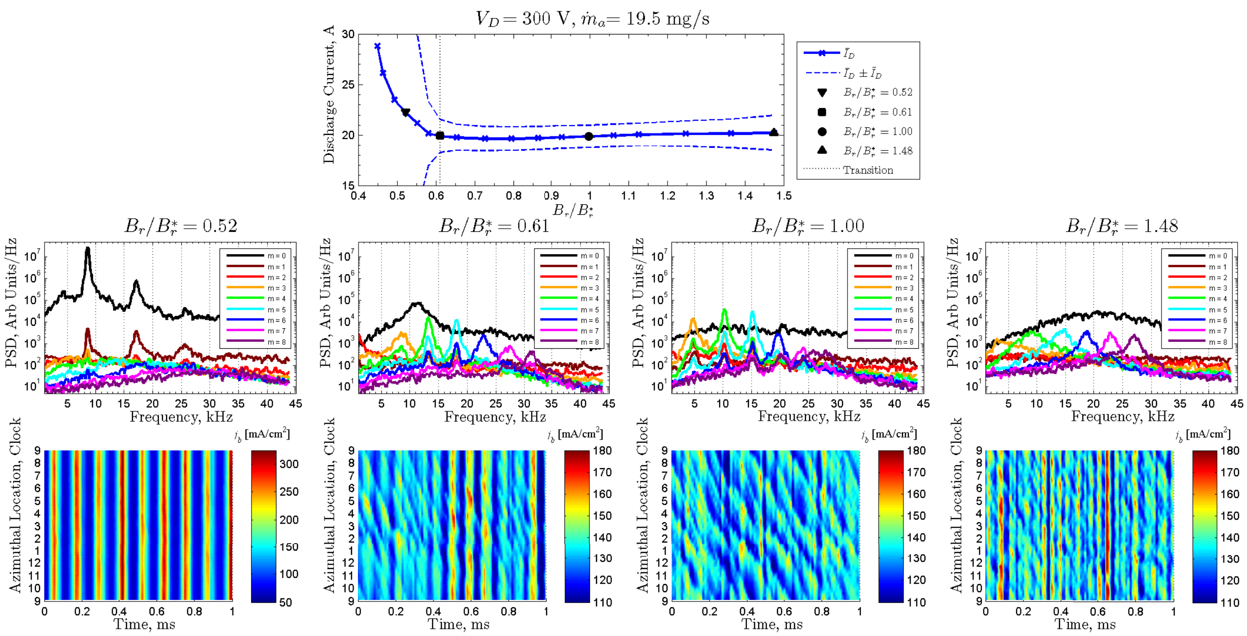

Fig. 3. B-field sweep for 300 V, 19.5 mg/s showing transition at $B_r/B_r^* = 0.61$. Top plot: mean discharge current (solid blue line) and oscillation amplitude (dashed blue line) with the mode transition (vertical dashed black line). Four B_r/B_r^* settings are selected for further analysis. Middle row plots: HIA PSDs showing the relative oscillation strength of the various spoke orders, m, with the black line representing m_0. A 500-Hz moving average filter has been applied to smooth all PSDs. Bottom row plots: discharge current density in the discharge channel for 1 ms. The scale range for discharge current density at $B_r/B_r^* = 0.52$ is larger owing to the magnitude of oscillations. Reproduced from [7, Fig. 17].

-30 V with respect to ground, which is more than 16 T_e below the plasma potential and therefore are safely in ion saturation. The ISR current is measured external to the LVTF across a 100 Ω shunt resistor through an Analog Devices AD 215 120-kHz low-distortion isolation amplifier. The data acquisition system used to record discharge current and the ISR signals are sampled at rates up to 180 MHz with 16-b AlazarTech ATS9462 digitizers.

C. Transition Results

The magnetic field B_r/B_r^* was varied by changing the inner and outer magnet coil currents in a constant ratio with all other parameters held constant including flow rates, discharge voltage, and chamber pressure. Maintaining a constant 1.12 ratio of inner to outer coil current allowed the magnetic field magnitude to be varied without changing the shape shown in Fig. 1. Decreasing B_r/B_r^* below a certain threshold was shown to repeatedly induce a mode transition where both the discharge current mean value and oscillation amplitude increased. An example of this transition is shown at the top of Fig. 3. The mean discharge current and oscillation amplitude (root-mean-square or RMS) are lowest in local mode ($B_r/B_r^* > 0.61$ and then increase sharply in global mode ($B_r/B_r^* < 0.61$). The transition point is $B_r/B_r^*|_{\text{trans}} = 0.61$. A defined transition B_r/B_r^* is misleading because there is a transition region where the plasma exhibits both types of oscillations as shown in Fig. 3; however, the transition typically occurred over only $\sim$10% change in B_r/B_r^*. Sekerak *et al.* [7] (Figs. 12–14) showed that $B_r/B_r^*|_{\text{trans}}$ increases with increasing flow rate and discharge voltage. The spokes shown in Fig. 3 for $B_r/B_r^* = 1.00$ and 1.48 are localized oscillations that are typically 10%–20% of the mean discharge current density value, while the oscillations in global mode $B_r/B_r^* = 0.52$ can be 100% of the mean value.

The modes are described in [7] as global oscillation mode and local oscillation mode. In global mode, the entire discharge channel plasma is oscillating in unison and spokes

This article has been accepted for inclusion in a future issue of this journal. Content is final as presented, with the exception of pagination.

are either absent or negligible with discharge current oscillation amplitude (RMS) greater than 10% of the mean value. Azimuthally spaced probes positioned downstream from the exit plane show no signal delay between each other and are very well correlated to the discharge current signal. In local oscillation mode, perturbations in the discharge current density are seen to propagate in the $E \times B$ direction with clear spokes shown in a HIA PSD. The discharge current oscillation amplitude and mean values are significantly lower than those observed in global mode. The azimuthally spaced probes in the plume show a clear signal delay between each other indicating the passage of spokes, but are not well correlated to the discharge current indicating localized plasma oscillations within the discharge channel. The mode transitions were consistent across different tests and showed no hysteresis, but did change at different operating conditions. The transition between global mode and local mode occurred at higher B_r/B_r^* for higher mass flow rate or higher discharge voltage. The investigation did not conclude a mechanism that caused mode transitions. The thrust was constant within experimental error through the mode transition, but the thrust-to-power ratio decreased by 25% for the 14.7 mg/s flow rate; the peak value of thrust-to-power occurred near the transition point. The plume showed significant differences between modes with the global mode significantly brighter in the channel and the near-field plasma as well as exhibiting a plasma spike on thruster centerline. It was concluded that the H6 and likely any similar thruster should be operated in local oscillation mode to minimize the discharge current mean value and amplitude of oscillations. Thruster performance maps should include variation in discharge current, discharge voltage, magnetic field, and flow rate to identify transition regions throughout the life of a thruster.

III. Spoke Velocity Measurements

The spoke velocity can be calculated from either the high-speed imaging or the azimuthally spaced probes by using several different methods. Spokes are observed to propagate at a range of velocities, so there is a distribution associated with the speed akin to a distribution function. The methods below will identify one representative velocity for spoke propagation.

A. Manual Method

Spokes are unambiguously observed in the FastCam videos as bright regions rotating azimuthally around the discharge channel as shown in Fig. 2. Using the McDonald technique to create a spoke surface [7], [15], the spokes appear as diagonal stripes in the spoke surface as shown in [7, Fig. 11]. This technique divides the discharge channel into 180 two-degree bins of averaged light intensity and a video consisting of N_{fr} frames will yield a $180 \times N_{\mathrm{fr}}$ spokes surface. The most obvious technique to calculate spoke velocity is to fit lines to the diagonal stripes on the spoke surface; the slope of which represent spoke angular velocity $\dot{\theta}_{\mathrm{sp}}$ in degree/s. In the FastCam videos and subsequent video enhancement [17, Figs. 2 and 3], spokes are observed to fill the entire

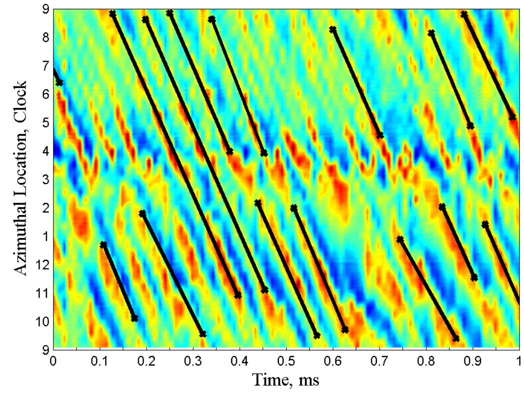

Fig. 4. One millisecond segment of a normalized spoke surface showing 14 of 47 manually fitted lines for $B_r/B_r^* = 1.00$.

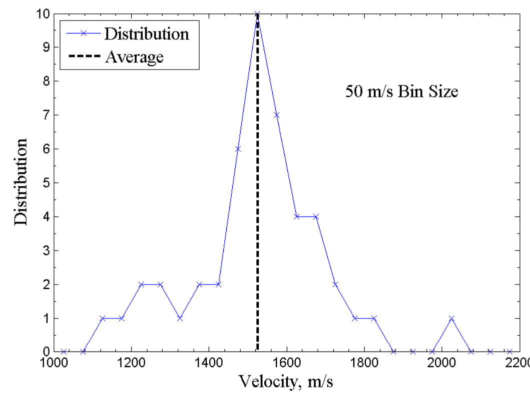

Fig. 5. Velocity distribution for the manually fitted lines in Fig. 4. Black dashed line: mean of the 47 measurements.

channel width. Therefore, spoke angular velocity is converted to a linear velocity using the mean channel radius, R_{chnl}

$$v_{\mathrm{sp}} = (2\pi R_{\mathrm{chnl}}/360)\,\dot{\theta}_{\mathrm{sp}}. \tag{1}$$

To determine an average spoke angular velocity, 45–50 lines are manually fitted to a normalized spoke surface as shown in Fig. 4 for $B_r/B_r^* = 1.00$, 300 V and 19.5 mg/s. A normalized spoke surface shows the spokes more clearly without altering their characteristic slope. To normalize a spoke surface, each frame (vertical line) has its mean value subtracted and is divided by its RMS value. To test the uncertainty due to human error and repeatability, approximately 50 lines were fitted to the same propagating spoke with a standard deviation of 39 m/s; this will be shown to be within the standard deviation of a typical velocity distribution. The velocity distribution for the spoke surface example of Fig. 4 is shown in Fig. 5 where the spoke velocity is 1530 $\pm$180 m/s and the uncertainty is the standard deviation of the distribution.

More sophisticated techniques will be introduced in later sections, but those results should be within the range of this straightforward, yet labor-intensive approach. Representative uncertainties for the manual method are the mean uncertainties shown in Fig. 9 of 190 and 180 m/s for 300 and 400 V, respectively.

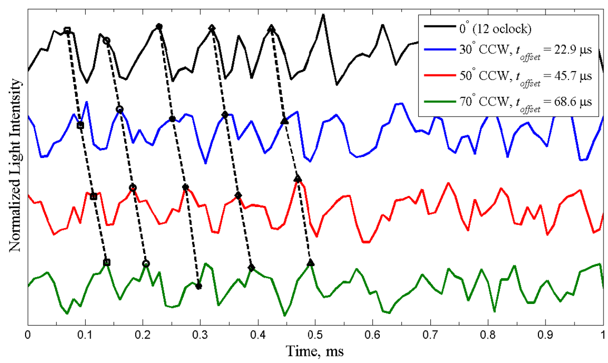

Fig. 6. Light intensity traces for four azimuthal locations from the normalized spoke surface in Fig. 4. Selected locations are thruster 12 o'clock as the reference and 30°, 50°, and 70° CCW from 12 o'clock. The offset times are calculated via linear cross correlation from 12 o'clock to the other locations. Five peaks have been selected to demonstrate how spokes propagate CCW around the thruster by using the calculated offset times.

B. Correlation Method

The correlation method uses linear cross-correlation to determine the time delay between oscillations in light intensity at different azimuthal locations in the discharge channel. The time delay represents transit time for a spoke to travel from one azimuthal location to another and is used to calculate angular and linear velocity. By comparing a large quantity of azimuthal locations ($\mathcal{O}10^3$) a representative spoke velocity can be calculated.

Starting with the normalized spoke surface as discussed earlier, the time-history signal of light intensity for each bin is a $1 \times N_{\mathrm{fr}}$ vector representing light fluctuations at that azimuthal location for the duration of the video, which is typically 150–250 ms ($N_{\mathrm{fr}} \sim 13 \times 10^3$ to 22×10^3). A 1 ms segment of four normalized light intensity traces are shown in Fig. 6. A linear cross-correlation analysis of the signals between two bins, b_j and b_k, at different azimuthal locations with an angular difference of $\Delta\theta_{j,k}$ degrees will yield the time, $t_{j,k}$, it took on average for a spoke to propagate around the channel from b_j to b_k. The cross-correlation function is [18]

$$R_{jk} = \lim_{T\to\infty} \frac{1}{T} \int_0^T b_j(t)\, b_k(t+\tau) dt. \tag{2}$$

Signal delays for nonfrequency dispersive propagation can be identified by peaks in R_{jk} where the highest peak is the time offset, $t_{j,k}$. Fig. 6 shows an example of the time offset for three azimuthal locations (30°, 50°, and 70°) referenced to 12 o'clock on the thruster face calculated from linear cross correlation. Five peaks in light intensity (spokes) are selected and shown how they propagate around the thruster in Fig. 6. The spoke velocity, $v_{spj,k}$, from b_j to b_k is

$$v_{spj,k} = (2\pi R_{\mathrm{chnl}}/360)\Delta\theta_{j,k}/t_{j,k}. \tag{3}$$

The spoke velocity for the correlation method is the mean spoke velocity calculated between N_{bins} compared

$$v_{\mathrm{sp}} = \frac{1}{N_{\mathrm{bins}}} \sum_j \sum_k v_{spj,k}. \tag{4}$$

In principle, the spoke velocity can be calculated from the average time delay using every combination of the 180 bins, which would be over 32 000. However, practical considerations limit the range of bins that can be compared. The camera frame rate is 87 500 frames/s so each frame represents 11.4 μs. A spoke traveling at 2000 m/s will travel 16° or 8 bins in the time span of one frame. Therefore, a practical lower limit is $\Delta\theta_{j,k} \geq 20°$ or ten bins. A single spoke typically propagates one-quarter of the discharge channel circumference for most B-field settings. In strong spoke regimes, a single spoke will propagate one-half to even the entire channel circumference. A reliable upper limit for automated processing is to only compare bins where $\Delta\theta_{j,k} \leq 70°$ or 35 bins. In Fig. 6, six cycles can be identified in ~0.55 ms, which corresponds to ~11 kHz or a spoke period of τ_{sp} ~90 μs. Because of signal noise, the cross-correlation peak occasionally matches to a spoke ahead or behind the correct spoke, so the calculated offset time is in error by one or two τ_{sp}. Although this occurs more often when $\Delta\theta_{j,k} > 90°$, it occasionally occurs for $\Delta\theta_{j,k} < 70°$. These points are easy to identify via manual inspection, but reject criteria is set for automated data processing, so any spoke velocity outside of 500–3500 m/s is rejected. To reduce computational time, only 90 bins (every other bin) are used for reference start points. All bins from bin 10 to 35 anticlockwise from the reference bin are used for comparison. Therefore, j is $1, 3, 5, \ldots$ to 180 and k is 10–35 in (4) which yields a maximum of $N_{\mathrm{bins}} = 2430$ possible points. The spoke velocities for smaller $\Delta\theta_{j,k}$ will have larger uncertainty because half of the camera frame period (5.7 μs) represents a large fraction of the spoke travel time (~14 μs to travel 20°). The standard deviation can be reduced choosing a larger value for the lower limit of $\Delta\theta_{j,k}$ instead of 20°, but the number of points used in the calculation, N_{bins}, will also be reduced, so a balance must be reached.

Using the correlation method on the spoke surface shown in Fig. 4 yields a spoke velocity of $v_{\mathrm{sp}} = 1470 \pm 270$ m/s where the uncertainty is the standard deviation of the velocities used in (4). This is within 4% of the manual technique described previously. For this data point, $N_{\mathrm{bins}} = 2266$ of the possible 2430 points are used for $20° \leq \Delta\theta_{j,k} \leq 70°$. The manual method and correlation method produce very similar results as shown later in Figs. 8 and 9. Representative uncertainties for the correlation method are the mean uncertainties shown in Fig. 9 of 280 and 260 m/s for 300 and 400 V, respectively. The correlation method is important because it is an automated and reliable procedure of providing the same results as the laborious manual method.

C. Dispersion Relation Method

Dispersion relations are common place in plasma physics to describe the relationship between oscillation frequency and wave number. This method determines the spoke velocity from the phase velocity of an empirically determined dispersion relation. The 2-D PSD identifies a peak frequency for each spoke order, which is equivalent to wave number, and thus yields a dispersion plot from high-speed imaging results. An assumed functional form is fit to the data to calculate the numerical values for the dispersion relation.

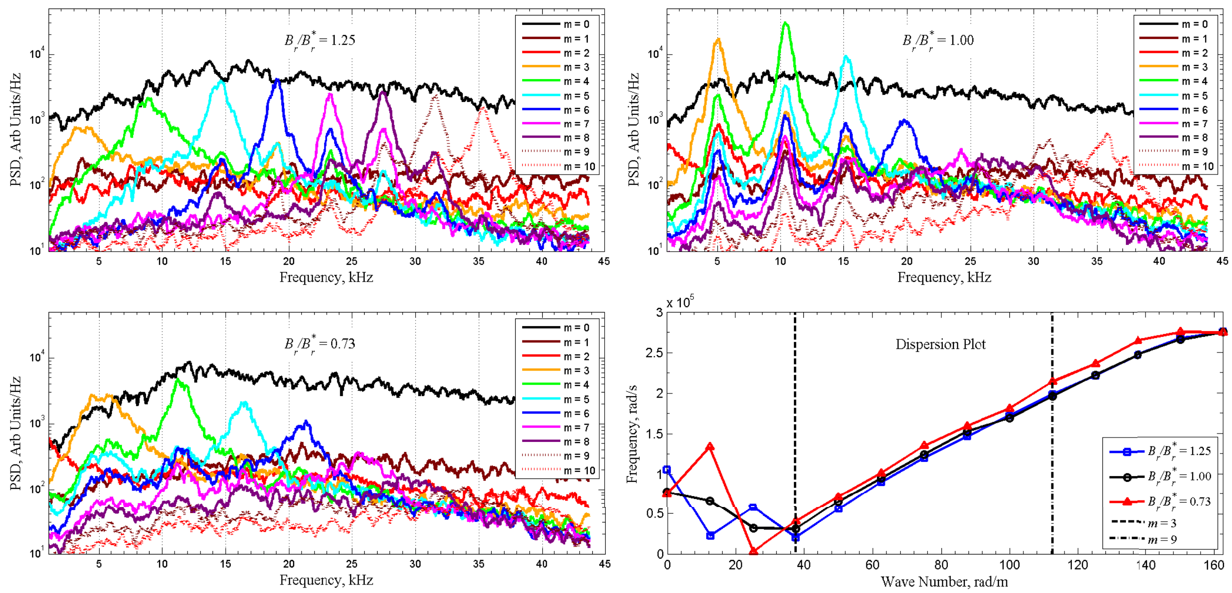

Fig. 7. HIA PSDs for $B_r/B_r^* = 1.25$, 1.00 and 0.73 for 300 V and 19.5 mg/s with $m = 0$–10 shown. A 500 Hz moving average window has been applied to each PSD trace to reduce noise. Bottom right: peak frequencies are identified and plotted versus wave number for corresponding dispersion relations.

The HIA method developed by McDonald [19] and described in detail in [7] generates PSDs from the 2-D spoke surface. Fig. 7 shows examples for the 300 V, 19.5 mg/s test case where peaks are clearly visible for each spoke order, m. As described by McDonald in his original derivation [15], m is analogous to number of wave lengths per channel circumference. Hence, $m = 0$ or m_0 is no wave in the channel (the entire channel is dark or bright), $m = 1$ means one wave in the channel (one half-bright, the other dark), $m = 2$ is two waves per channel (two bright regions, two dark regions), $m = 3$ is three waves per channel (three bright regions, three dark regions), and so on. In the literature m is often called the wave mode, but we call it spoke order to avoid nomenclature confusion with the HET operational modes discussed in Section II. The azimuthal wave number, k_θ, is calculated from the spoke order by $k_\theta = m/r$. Fig. 7 shows each spoke order has a unique peak frequency that is typically 3–5 kHz higher than the previous m. Therefore, the HIA PSDs can be used to generate dispersion plots of peak frequency ω versus wave number k_θ.

The HIA PSDs are a powerful tool for understanding the plasma oscillations associated with HET operation. Sekerak *et al.* [20] showed that the ISR probes identified the same peak frequencies as the HIA PSDs indicating that spoke-related oscillations extended out into the plume. The same spoke surface that generated the normalized spoke surface as shown in Fig. 4 was used to generate the HIA PSD for $B_r/B_r^* = 1.00$ as shown in Fig. 7. Note the most dominant peak for $B_r/B_r^* = 1.00$ is $m = 4$ at 10.4 kHz, which is close to the crudely estimated frequency as shown in Fig. 6 of ~11 kHz.

To automatically identify the peak frequencies for each spoke order, the PSDs are first smoothed with a 250 Hz moving average filter and the maximum value identified. Because of noise from the Fourier transform, the maximum value is not always the frequency at the center of the peaks shown in Fig. 7, so a Lorentzian [21] of the form

$$\mathrm{PSD}(f) = \frac{A_0}{\pi} \frac{\frac{1}{2}\Gamma}{(f - f_0)^2 + \left(\frac{1}{2}\Gamma\right)^2} \quad (5)$$

is fitted to a segment of the PSD around the maximum value. The fit variables in (5) are the full-width at half-maximum Γ, amplitude A_0, and center frequency f_0. This identifies the frequency f_0 or ω_0 at the center of the primary peak for each m. Example dispersion plots using this technique for the three HIA PSDs are also shown in Fig. 7.

For high magnetic field strength, $B_r/B_r^* = 1.25$, the higher spoke orders are most prominent with $m = 10$ showing a peak near the same height as $m = 5$. At the nominal setting, $B_r/B_r^* = 1.00$, the spoke orders $m = 3$–5 are an order of magnitude higher than $m \geq 6$, although peaks are visible up to $m = 10$. At the lowest magnetic field setting, $B_r/B_r^* = 0.73$, spoke orders $m = 3$–5 are still dominant but lower in magnitude than $B_r/B_r^* = 1.00$. Although very weak, peaks are still visible for $m = 6$–9. As magnetic field is increased, the frequency of each spoke order decreases as shown in the PSDs and dispersion plot shown in Fig. 7.

First-principles-based dispersion relations are derived from linearized, plasma physics equations and represent physical mechanisms for given oscillations. The empirical relationship between ω and k_θ shown in Fig. 7 does not offer any physical explanation for the cause of the azimuthal oscillations. To gain insight into the physical mechanisms behind spokes, a functional form is selected to fit the data and coefficients calculated from least-squared fits are compared with coefficients from physics-based dispersion relations. The chosen empirical dispersion relation functional form most likely will not exactly replicate a first-principles-derived dispersion relation, but similarities between them may be insightful. A first-principles-derived dispersion relation that explains spokes should reduce to a form similar to the empirical relation by using a set of assumptions or approximations. With the preceding discussion in mind, several functional forms that can represent the empirical relationship between ω and k_θ shown in Fig. 7 include

$$\omega^\alpha = v_{\rm ch}^\alpha k_\theta^\alpha - \omega_{\rm ch}^\alpha \tag{6}$$

$$\omega = -v_{ch2}^2 k_\theta^2 + v_{ch1} k_\theta - \omega_{\rm ch} \tag{7}$$

$$\omega = \sqrt{\omega_{\rm ch}(v_{\rm ch} k_\theta - \omega_{\rm ch})} \tag{8}$$

where (6) is a power law relation and $\alpha = 1$ recovers a simple linear relationship, (7) is a second-order polynomial and (8) is a parabola. These functional forms do not constitute an exhaustive list of all possible functional forms, but they all share an important characteristic that ω is monotonically increasing with k_θ over the expected range of k_θ shown in Fig. 7. The negative signs in (6)–(8) are the result of least-square fits. The coefficients have been written as characteristic velocities, $v_{\rm ch}$, and characteristic frequencies, $\omega_{\rm ch}$. These have been calculated from a least-square fit to the $m = 3$–9 spoke order data for $B_r/B_r^* = 1$ shown in Fig. 7 with the results shown in (9)–(13). Note that $\alpha = 1, 2$, and 3 have been separately calculated for the power law in (9)–(11), respectively

$$\omega = (2170)k_\theta - (4.40 \times 10^4) \tag{9}$$

$$\omega^2 = (1820)^2 k_\theta^2 - (6.05 \times 10^4)^2 \tag{10}$$

$$\omega^3 = (1760)^3 k_\theta^3 - (7.11 \times 10^4)^3 \tag{11}$$

$$\omega = -(2.87)^2 k_\theta^2 + (3410)k_\theta - (8.52 \times 10^4) \tag{12}$$

$$\omega = \sqrt{(1.43 \times 10^5)((3500)k_\theta - 1.43 \times 10^5)}. \tag{13}$$

The power law relation of (6) displays the smallest deviations for all values, including those outside the range of $m = 3$–9. The parabolic relation from (8) and (13) has the largest deviations from the data. Except for the second-order coefficient of (12) at 2.87 m/s, the characteristic velocities for each functional form are the same order of magnitude in the range 1760–3500 m/s. It is interesting to note this velocity range corresponds to ion acoustic speeds with 4–17 eV electrons commonly observed in HET discharge channels and plumes, which is discussed in Section IV-C. The characteristic frequencies show excellent similarities with a range 4.40–14.3 $\times 10^4$ rad/s. The power law relation in (6) with $\alpha = 1$ and 2 will be used for further analysis owing to its simplicity and because it provides the best fit for the largest range of k_θ and ω.

The unexpected minus sign in (6)–(8) results from the ordinate intercept shown in Fig. 7, which is $\omega < 0$ when extrapolating backwards for $m < 2$ by using the points from $3 \leq m \leq 12$. The physical implication is a limit of $v_{\rm ch}^\alpha k_\theta^\alpha > \omega_{\rm ch}^\alpha$ for ω to be real in (6), so the only spoke orders that can exist are

$$m > R_{\rm chnl}\frac{\omega_{\rm ch}}{v_{\rm ch}} = m_{\rm min}. \tag{14}$$

In practice, $m_{\rm min}$ is typically 3 or 4. The phase velocity, $v_{\rm ph}$, and group velocity, $v_{\rm gr}$, from the dispersion relation in (6) are

$$v_{\rm ph} = \frac{\omega}{k_\theta} = \left[v_{\rm ch}^\alpha - \left(\frac{\omega_{\rm ch}}{k_\theta}\right)^\alpha\right]^{1/\alpha} \tag{15}$$

$$v_{\rm gr} = \frac{\partial\omega}{\partial k_\theta} = v_{\rm ph}\left(\frac{v_{\rm ch}}{v_{\rm ph}}\right)^\alpha. \tag{16}$$

Equation (15) shows that the phase velocity will always be less than the characteristic velocity and (16) shows the group velocity will always be greater than the phase velocity. In the limit of $(\omega_{\rm ch}/(k_\theta v_{\rm ch}))^\alpha \ll 1$ that follows from (14), a binomial expansion of (15) yields a simplified phase velocity

$$v_{\rm ph} \simeq v_{\rm ch}\left[1 - \frac{1}{\alpha}\left(\frac{\omega_{\rm ch}}{k_\theta v_{\rm ch}}\right)^\alpha\right] = v_{\rm ch}\left[1 - \frac{1}{\alpha}\left(\frac{m_{\rm min}}{m}\right)^\alpha\right]. \tag{17}$$

With the FastCam frame rate at 87 500 frames/s the Nyquist limit is 43.8 kHz (2.75×10^5 rad/s), which is the asymptotic peak value for $m \geq 12$ observed in the dispersion plots shown in Fig. 7. In fitting the simple dispersion relation of (6) to the data shown in Fig. 7, a parametric study was done to determine the limits on m. Three different ranges were selected for spoke orders: $3 \leq m \leq 8, 9, 10$. In general, the results were not sensitive to the upper limit of m used, but the $m = 8$ case had more variation in characteristic velocity. For all future comparison plots, the range of m used for curve fitting will be $m = 3$–9 and $\alpha = 1, 2$ in (6).

The aforementioned manual and correlation methods both identify a single, dominant spoke velocity for a given magnetic field setting and operating condition. However, the phase velocity from (15), which is assumed to be the spoke velocity, is a function of wave number. Fig. 8 shows $v_{\rm ph}$ as a function of spoke order m as a proxy for k_θ for 300 and 400 V and $\alpha = 1, 2$ ($\alpha = 3$ is very similar to $\alpha = 2$ and is not shown). A single, representative spoke velocity can be calculated from a weighted average spoke velocity by using the PSD value at the peak frequency f_m as the weighting factor w_m for each m. The spoke velocity and weighting factors are

$$v_{\rm sp} = \sum_{m=5}^{9} \mathrm{w}_m v_{\rm ph} \tag{18}$$

$$\mathrm{w}_m = \frac{\mathrm{PSD}(f_m)}{\sum_{m=5}^{9}\mathrm{PSD}(f_m)}. \tag{19}$$

The HIA PSDs shown in Fig. 7 show that certain spoke orders are dominant at different magnetic field settings, with spoke orders $m = 4$ and 5 are dominant for $B_r/B_r^* < 1.0$. Fig. 8 shows that for 300 V the phase velocities for $m = 3$ are far too low and for 400 V the phase velocities for $m = 3$ and 4 are too low. The higher spoke orders are either dominant or the same magnitude as $m = 4, 5$ for the higher magnetic field settings. The weighting method of (19) accounts for the higher spoke order dominance at higher B_r/B_r^* values and causes the upward shift above ∼1, which tracks very well with the spoke velocities calculated via the manual and correlation method and builds confidence in the dispersion method. The minimum spoke order $m = 5$ was chosen in (18) and (19) such that (14)

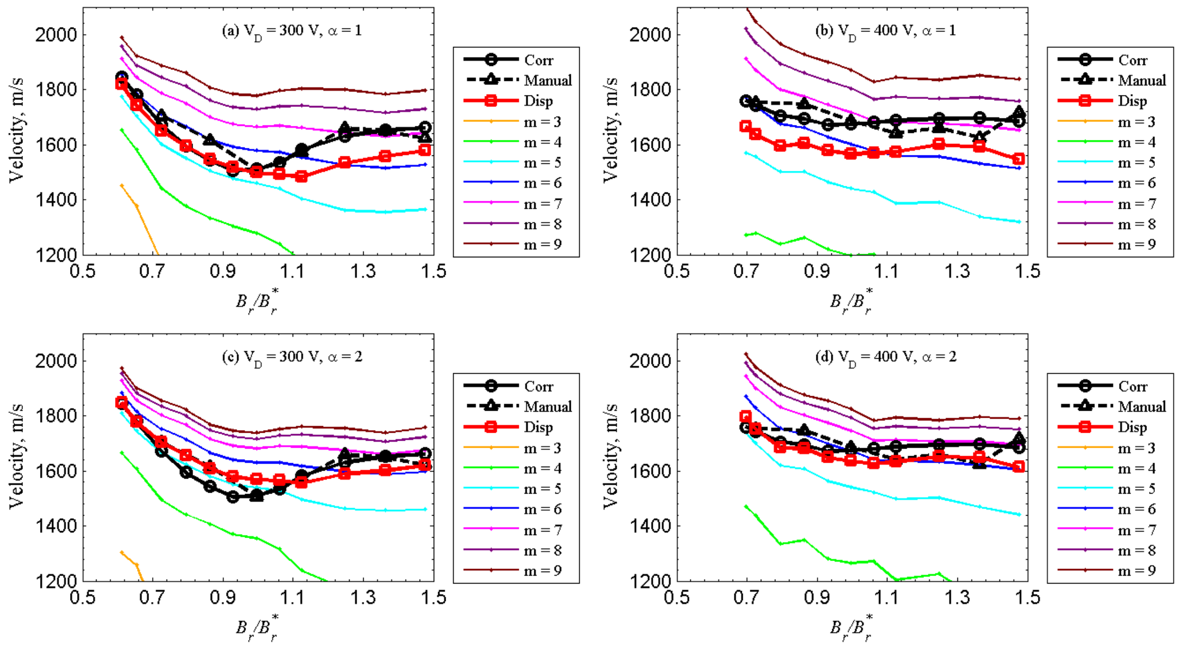

Fig. 8. Comparison of phase velocities and spoke velocities for (a) and (c) 300 V and (b) and (d) 400 V, 19.5 mg/s for (a) and (b) $\alpha = 1$ and (c) and (d) $\alpha = 2$. Colored lines: phase velocity for each spoke order m calculated with (15). Red lines: squares are spoke velocities calculated with the dispersion method and (18). Solid black lines: circles are spoke velocities calculated using the correlation method. Dashed black lines: triangles are spoke velocities calculated using the manual method.

is satisfied for all conditions. Fig. 8 shows the velocity from the correlation method typically follows the phase velocity for $m = 5$ or 6 closely for $B_r/B_r^*|_{\text{trans}} \leq B_r/B_r^* \lesssim 1.0$ and for $B_r/B_r^* \gtrsim 1.0$ the correlation velocity follows $m \geq 6$. Therefore, using the phase velocities for $5 \leq m \leq 9$ to calculate a representative spoke velocity is reasonable. Using $4 \leq m \leq 12$ yields the same shape, but shifted lower by 100–200 m/s. Fig. 8 shows for 300 V both $\alpha = 1$ and 2 yield spoke velocities from the dispersion method that match the manual and correlation methods, but $\alpha = 2$ is better correlated for 400 V.

The uncertainty in phase velocity from (15) for wave number k_θ is calculated using the standard error for the fit coefficients [22] and the error propagation equation [23]. The total uncertainty in spoke velocity is calculated using the weighted average technique of (18) and (19). For the same example shown in Fig. 4 of $B_r/B_r^* = 1$, 300 V and 19.5 mg/s, the spoke velocity is 1510 ± 140 m/s for $\alpha = 1$ and 1570 ± 60 m/s for $\alpha = 2$. This is within 4% of the spoke velocity calculated with the manual method. Representative uncertainties for the dispersion relation method are the mean uncertainties shown in Fig. 9 of 120 and 47 m/s for $\alpha = 1$ and 2 at 300 V, and 157 and 41 m/s for $\alpha = 1$ and 2 at 400 V.

D. Probe Delay Method

A final method to calculate spoke velocity is to calculate the time delay with linear cross correlation of a signal passing from one azimuthally spaced probe to another. The downstream probes are azimuthally separated on channel centerline and observe the same plasma oscillations with a time delay. This time offset is converted to linear velocity based on the probe azimuthal spacing.

The ISR probes are used to measure plasma oscillations in the plume that correlate to light intensity oscillations in the discharge channel. As discussed at length in [7], both ISR probes observed the same plasma oscillations, but in local mode the signal was delayed, whereas in global mode the oscillations occurred nearly simultaneously at each probe. The time delay, t_d, was determined from a linear cross-correlation technique described in Section III-B and (2). As shown in [7, Fig. 20(c)], the time delay in local mode was between 10 and 15 μs.

The spoke velocity can be calculated from the linear, azimuthal distance between each probe, $L_{\text{pr}} = (2\pi R_{\text{chnl}}/360)\,\Delta\theta_{1,2}$, divided by the time delay

$$v_{\text{sp}} = L_{\text{pr}}/t_d. \tag{20}$$

The uncertainty in L_{pr} is calculated from the probe spacing uncertainty of 1.7° and the uncertainty of t_d is assumed to be 10% of the value [16]. These uncertainties are used to calculate the maximum and minimum values for spoke velocity at a given setting $v_{\text{sp}}|_{\min}^{\max} = (L_{\text{pr}} \pm \sigma_{\text{Lpr}})/(t_d \mp \sigma_{td})$. For the sample data point used in the previous methods of $B_r/B_r^* = 1.00$, 300 V, and 19.5 mg/s, the spoke velocity is 2090 ± 380 m/s, which is 38% higher than the spoke velocity calculated via the manual method. Representative uncertainties for the probe delay method are the mean uncertainties shown in Fig. 9 of 390 and 420 m/s for 300 and 400 V, respectively.

IV. Discussion

A. Spoke Velocity Comparison

Fig. 9 shows the spoke velocity calculated via all four methods discussed above with error bars for 300 and 400 V at 19.5 mg/s flow rate. The manual, correlation, and dispersion

This article has been accepted for inclusion in a future issue of this journal. Content is final as presented, with the exception of pagination.

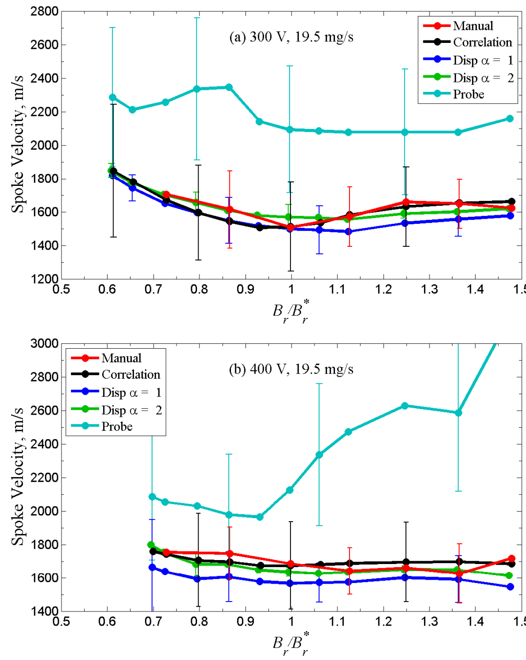

Fig. 9. Comparison of spoke velocity calculation methods: manual, correlation, dispersion relation with $\alpha = 1, 2$, and probe delay method for (a) 300 V and (b) 400 V. Not all error bars are shown for clarity. For the dispersion relations, $m \geq 5$ has been used in (18) and (19).

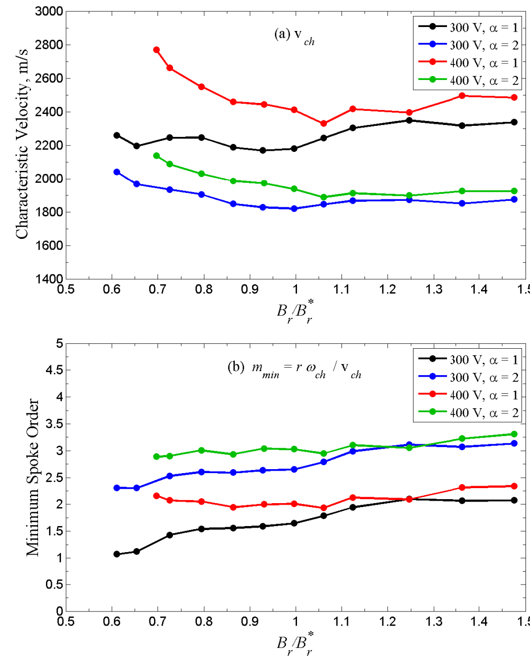

Fig. 10. Comparison of (a) characteristic velocity v_{ch} and (b) minimum spoke order from (14) for 300 and 400 V, 19.5 mg/s. Power dependence $\alpha = 1$ and 2 are considered.

methods are all very well correlated. The spoke velocity from probe delay is consistently higher by ~30% for both conditions with the 400 V condition showing an unusual rise for $B_r/B_r^* > 0.9$. The reason for this divergence is unknown. The spoke velocity is initially inversely dependent on B_r/B_r^* until $B_r/B_r^* \sim 1$ then levels out for higher magnetic field strength. The inverse dependence of v_{sp} on B_r/B_r^* is stronger for the 300 V condition than 400 V. Fig. 10 shows the characteristic velocities and m_{min} for the dispersion method for 300 V, 400 V, and $\alpha = 1$ and 2. The characteristic velocities are higher for the $\alpha = 1$ and for $\alpha = 2$ they show the same inverse dependence on B_r/B_r^* until ~1, after which they become level at the same value. The minimum spoke order appears to be linearly dependent on B_r/B_r^* with $\alpha = 2$ higher.

Fig. 11 shows a comparison of spoke velocities calculated from the correlation method for all five conditions tested. The 300 V, 19.5 mg/s condition is the average of four sweeps and the 400 V, 19.5 mg/s condition is the average of two sweeps. All conditions show the same trend of spoke velocity inversely dependent on B_r/B_r^* until $B_r/B_r^* \sim 1$. Power dependencies of $v_{\mathrm{sp}} \propto (B_r/B_r^*)^{-0.5}$ and $v_{\mathrm{sp}} \propto (B_r/B_r^*)^{-0.25}$ are shown in Fig. 11 for reference purposes only and were not generated from curve fits. The 300 V, 19.5 mg/s, and 14.7 mg/s conditions show the strongest inverse dependence closer to the -0.5 reference, all others are closer to the -0.25 reference. For $B_r/B_r^* \gtrsim 1$, the 300 V, 14.7 mg/s condition still decreases, but not as steeply and 300 V, 19.5 mg/s actually increases velocity before stabilizing. All other conditions are essentially constant for the higher magnetic field settings. With the exception of 300 V, 14.7 mg/s, all conditions asymptote between 1600 and 1700 m/s for the maximum magnetic field settings. The trend of decreasing spoke velocity with increasing B_r/B_r^* for $B_r/B_r^* \lesssim 1$ is clear, but the velocity change is small, typically <25%. The variation in spoke velocity during a magnetic field sweep is on the order of the uncertainty shown in Fig. 9, reinforcing that the dependence on magnetic field magnitude is not strong. Therefore, the spoke velocity is weakly inversely dependent or completely independent of magnetic field strength in the H6 at the conditions tested.

The $E \times B$ drift velocity is calculated in the H6 discharge channel by using the internal plasma measurements of Reid [24]. The maximum value is over 4×10^6 m/s at the peak electric field and of order 10^5 m/s within $\pm 0.2 L_{\mathrm{chnl}}$ centered on the peak. These velocities are two to three orders of magnitude higher than the typical spoke velocity of 1500–2200 m/s. The electric field would have to be small, $E_z \sim 0.01$ V/mm, for $v_{E\times B} \sim v_{\mathrm{sp}}$. Assuming the electrons follow a circular path on channel centerline during the azimuthal drift, they would circle the thruster in 0.13 μs (8 MHz) at the peak $v_{E\times B}$ and 26 μs (38 kHz) upstream from the ionization region. It should be noted the electron thermal velocity, υ_{the}, is an order of magnitude or larger than the $E \times B$ drift velocity throughout most of the channel and plume, except at the axial location of peak electric field.

Spokes are always observed to propagate in the $E \times B$ drift direction[2] indicating they are likely related to the azimuthal Hall current, which has an azimuthal velocity of $v_{E\times B} = E_z/B_r$. Using the steady-state, perpendicular velocity component from the electron fluid equation of motion and neglecting

[2]Personal correspondence with McDonald. During a test in July 2009, the polarity of the H6 magnets were reversed while the thruster was running at $V_D = 300$ V, $I_D = 10$ A, and $B_r/B_r^* = 0.70$, and the spokes were observed with the FastCam to change directions. Videos of one-fourth of the discharge channel were acquired at 54 000 frames/s.

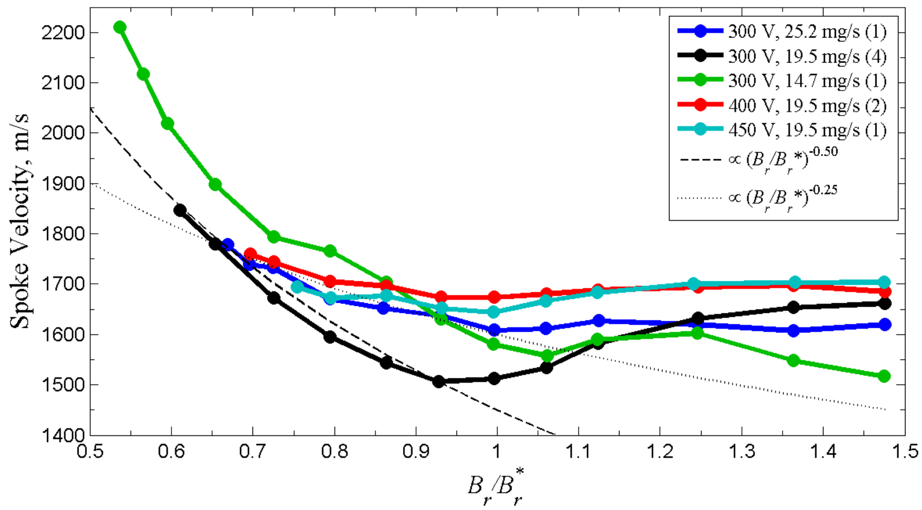

Fig. 11. Spoke velocity calculated with the correlation method for all conditions tested. Parenthetical numbers are the number of B-field sweeps averaged together. Reference lines for possible functional forms of v_{sp} dependence on B_r/B_r^* are shown for discussion purposes only.

the density and temperature-gradient terms, the axial electric field can be written as

$$E_z \approx \eta_\perp \; j_D \approx \left(1+\Omega_e^2\right)\eta \; j_D \approx \frac{B_r^2}{m_e \nu_{\text{ef}} n} j_D \tag{21}$$

which is Ohm's law where the cross field, $\eta_\perp$, and classical, η, resistivities are

$$\eta_\perp = \left(1+\Omega_e^2\right)\eta \quad \eta = \frac{m_e \nu_{\text{ef}}}{q^2 n}. \tag{22}$$

In addition, n is the plasma density, m_e is the electron mass, ν_{ef} is the effective collision frequency, j_D is the discharge current density, $\Omega_e = \omega_{\text{ce}}/\nu_{\text{ef}}$ is the Hall parameter, and $\omega_{\text{ce}} = qB/m_e$ is the electron cyclotron frequency. The second approximation in (21) uses the assumption that $\Omega_e \gg 1$, which is justified as the Hall parameter is known to be between 200 and 800 in the ionization region of HETs [25]. Equation (21) shows how the electric field is formed from the magnetic field, which creates high cross-field resistivity in the plasma. The large resistance created by the magnetic field also heats the plasma through Joule heating. The peak electron temperature in a HET discharge is typically ~30 eV, whereas the rest of the plasma is <10 eV. The dependence of E_z on B_r in (21) implies the $E \times B$ drift velocity in HETs scales as

$$v_{E\times B} = \frac{E_z}{B_r} \approx \frac{B_r}{m_e \nu_{\text{ef}} n} j_D. \tag{23}$$

The linear scaling between $v_{E\times B} \propto B_r$ is counter to the inverse scaling that is intuitively expected $v_{E\times B} \propto 1/B_r$ if E_z and B_r are independent. The assumption of nearly constant j_D with varying B_r is justified in local mode as shown in Fig. 3 and [7, Figs. 12 and 13] where the discharge current is constant to within 5% before the mode transition to global mode. In summary, any proposed theory for spokes must account for the observation that spokes propagate in the $E \times B$ direction, yet do not have the same velocity magnitude or scaling characteristics with magnetic field strength as the Hall current.

B. Spoke Velocity Observation Limits

Each spoke order represents the number of light and dark regions in the thruster, which is the wavelength $\lambda = 2\pi R_{\text{chnl}}/m$. If the spoke travels a half-wavelength during the period of time the shutter is open, then the bright region will travel over the dark region rendering the spoke unobservable by the camera. Assuming the open period of the shutter is $\tau_s = 1/f_c$ where f_c is the camera frame rate, then the observable spoke velocity is

$$v_{\text{sp}} < \frac{\pi R_{\text{chnl}} f_c}{m}. \tag{24}$$

For $m = 3, 5, 7$, and 9, (24) yields maximum observable spoke velocities of 7300, 4400, 3100, and 2400 m/s, respectively. This is within all of the spoke velocities for each spoke order as shown in Fig. 8; however, the highest spoke orders are close to the limit.

C. Ion Acoustic Speed and Electrostatic Ion Cyclotron Waves

Plasma measurements internal to the discharge channel were made by Reid [24] on the H6 at 300 V with 20 mg/s anode flow rate after less than 300 h of total thruster operation. The magnet settings used were $I_{\text{IM}} = 3$ A and $I_{\text{OM}} = 2.68$ A, which corresponds to $B_r/B_r^* = 0.86$. The spoke velocity is 1540 m/s as shown Fig. 11 for $B_r/B_r^* = 0.86$ and the characteristic velocities are 2190 and 1850 m/s for $\alpha = 1$ and 2 as shown Fig. 10(a). Fig. 12 shows a comparison of those velocities with the channel centerline ion acoustic velocity, $\upsilon_s = \sqrt{(qT_e/m_i)}$, and the critical ionization velocity, υ_{ci}. The ion acoustic speed for $T_e = 5$ eV is 2000 m/s and for $T_e = 35$ eV is 5000 m/s. Janes and Lowder [1] suggested that the spokes may be related to the critical ionization velocity first proposed by Alfvén. The critical ionization velocity for xenon shown in Fig. 12 is 4200 m/s, which is the same order of magnitude as the spoke velocity, but is still over twice the value. The ion acoustic speed matches the characteristic speed for $\alpha = 2$ better than $\alpha = 1$, particularly for $z/L_{\text{chnl}} < 0.7$.

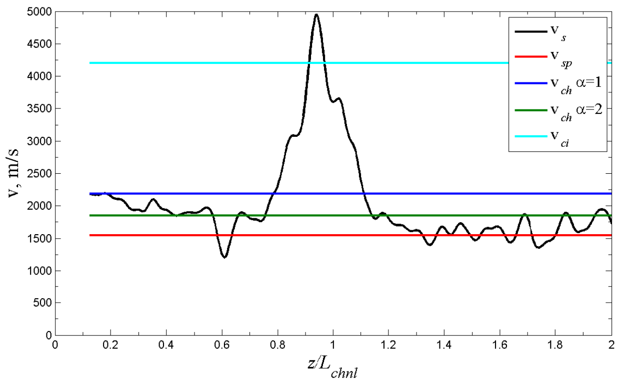

Fig. 12. Ion acoustic speed on channel center line for $B_r/B_r^* = 0.86$ calculated from data presented in [24] and smoothed by a 0.038 z/L_{chnl} moving average filter. The critical ionization velocity, spoke velocity, and characteristic velocities for $\alpha = 1, 2$ are shown for comparison.

The spoke velocity is lower than the ion acoustic speed in the near-anode region, but is similar to the near-field plume region.

An electrostatic ion cyclotron wave [26] is similar to an ion acoustic oscillation except the Lorentz force provides a restoring force [27], which yields the following dispersion relation:

$$\omega^2 = k^2 v_s^2 + \omega_{ci}^2 \tag{25}$$

this needs to be moved up where v_s is first discussed. Electrostatic ion cyclotron waves can propagate nearly perpendicular to B and has a phase velocity of

$$v_{\text{ph}} = \sqrt{v_s^2 + \omega_{ci}^2/k^2}. \tag{26}$$

Except for the difference in sign inside the radical, note the similarity to (15) with $\alpha = 2$, the ion acoustic speed as the characteristic velocity, and the ion cyclotron frequency as the characteristic frequency. Because the spoke location is unknown, spokes could be related to electrostatic ion cyclotron waves in the channel near the anode or in the near-field plume region where $T_e \sim 5$ eV.

The observation that ion acoustic speeds in some regions of the discharge channel match the characteristic speed from the dispersion method is encouraging, because v_s commonly appears in waves such as the electrostatic ion cyclotron wave and arises prominently in drift waves. In Escobar's simplified model that includes ionization [28], the wave speed was found to be of order the ion acoustic speed and Cavalier recently found modes that resemble ion acoustic waves [29]. However, it should be cautioned that the location and mechanism for spokes are still unknown, and any similarities between spokes and ion acoustic waves are currently circumstantial.

D. Observation of Spoke Characteristics

Combining the above discussion, we can state the following observations regarding spoke velocities in the H6. Any theory on spoke mechanisms and propagation should account for these results when applied to the specific geometry and magnetic field topology of the H6.

1) Propagation is in the $E \times B$ direction. Reversal of the magnet field direction will cause the spokes to propagate in the opposite direction.
2) Predict a spoke velocity of 1500–2200 m/s in the H6. Spoke velocities are not dependent on discharge voltage or mass flow rate to within experimental error for $V_D = 300$–450 V and $\dot{m}_a = 14.7$–25.2 mg/s. Spoke velocity dependence on thruster size is unknown, although likely weak as noted by McDonald [6]. These velocities are two to three orders of magnitude smaller than the $E \times B$ drift velocity of the azimuthal Hall current.
3) The dispersion relation can be approximated by a power law dependence $\omega^\alpha \sim v_{\text{ch}}^\alpha k_\theta^\alpha - \omega_{\text{ch}}^\alpha$ where $\alpha \geq 1$. The spoke velocity v_{sp} is less than the characteristic velocity v_{ch} and is dependent on the dominant spoke orders, typically $m > 4$. In general, the dominant spoke order increase with increasing magnetic field strength.
4) Spoke velocity should either be independent or weakly, inversely dependent on magnetic field strength. For the H6 an example dependence of $v_{\text{sp}} \propto B^{-\beta}$ where $0.25 \lesssim \beta \lesssim 0.5$ is shown in Fig. 11 for $B_r/B_r^*|_{\text{trans}} < B_r/B_r^* \lesssim 1$, but other functional forms are possible. For $B_r/B_r^* \gtrsim 1$, the spoke velocity nearly asymptotes to a constant value. This differs from the $E \times B$ drift velocity of the azimuthal Hall current, which is expected to approximately scale as $v_{E\times B} \propto B_r$.
5) Spokes are not observed in magnetically shielded thrusters [30] except for very high magnetic field strengths as discussed in [14, Appendix C].

V. Conclusion

The spoke velocity is determined using three methods with similar results: manual fitting of diagonal lines on the spoke surface, linear cross correlation between azimuthal locations, and an approximated dispersion relation. The spoke velocity in the H6 for three discharge voltages (300, 400, and 450 V) and three anode mass flow rates (14.7, 19.5, and 25.2 mg/s) are between 1500 and 2200 m/s across a range of normalized magnetic field settings. The spoke velocity is inversely dependent on magnetic field strength for $B_r/B_r^* \lesssim 1$ and asymptotes to 1600–1700 m/s for $B_r/B_r^* \gtrsim 1$ for all conditions except 300 V, 14.7 mg/s. Spoke velocity from a fourth method, the probe delay method, is ~30% higher for 300 V, 19.5 mg/s, and for 400 V, 19.5 mg/s shows an unexplained increase for $B_r/B_r^* > 0.9$. The empirically approximated dispersion relation of $\omega^\alpha = v_{\text{ch}}^\alpha k_\theta^\alpha - \omega_{\text{ch}}^\alpha$ where $\alpha \geq 1$ yields a characteristic velocity that matches the ion acoustic speed for ~5 eV electrons that exist in the near-anode and near-field plume regions of the discharge channel. These detailed observations of azimuthal spoke propagation are distilled into a list of criteria any potential theory for spoke mechanics must explain.

Acknowledgment

The authors would like to thank M. McDonald for development of the FastCam Analysis and B. Reid for his internal measurements. They would also like to thank M. Georgin for his tedious manual spoke velocity calculations.

REFERENCES

[1] G. S. Janes and R. S. Lowder, "Anomalous electron diffusion and ion acceleration in a low-density plasma," *Phys. Fluids*, vol. 9, no. 6, p. 1115, 1966.

[2] Y. Raitses, M. Griswold, L. Ellison, J. Parker, and N. Fisch, "Studies of rotating spoke oscillations in cylindrical Hall thrusters," in *Proc. AIAA*, Atlanta, GA, USA, Aug. 2012.

[3] C. L. Ellison, Y. Raitses, and N. J. Fisch, "Cross-field electron transport induced by a rotating spoke in a cylindrical Hall thruster," *Phys. Plasmas*, vol. 19, no. 1, p. 013503, 2012.

[4] J. B. Parker, Y. Raitses, and N. J. Fisch, "Transition in electron transport in a cylindrical Hall thruster," *Appl. Phys. Lett.*, vol. 97, no. 9, pp. 091501-1–091501-3, Aug. 2010.

[5] D. Brown and A. Gallimore, "Investigation of low discharge current voltage Hall thruster operating modes and ionization processes," in *Proc. IEPC*, Ann Arbor, MI, USA, Sep. 2009.

[6] M. S. McDonald and A. D. Gallimore, "Parametric investigation of the rotating spoke instability in Hall thrusters," in *Proc. 32nd Int. Electr. Propuls. Conf. (IEPC)*, Wiesbaden, Germany, Sep. 2011.

[7] M. J. Sekerak, R. R. Hofer, J. E. Polk, B. W. Longmier, A. D. Gallimore, and D. L. Brown, "Mode transitions in Hall effect thrusters," in *Proc. 49th AIAA/ASME/SAE/ASEE Joint Propuls. Conf.*, Jul. 2013.

[8] A. I. Morozov, "The conceptual development of stationary plasma thrusters," *Plasma Phys. Rep.*, vol. 29, no. 3, pp. 235–250, Mar. 2003.

[9] G. N. Tilinin, "High-frequency plasma waves in a Hall accelerator with an extended acceleration zone," *Soviet Phys.-Tech. Phys.*, vol. 22, no. 8, pp. 974–978, Aug. 1977.

[10] N. Gascon, M. Dudeck, and S. Barral, "Wall material effects in stationary plasma thrusters. I. Parametric studies of an SPT-100," *Phys. Plasmas*, vol. 10, no. 10, p. 4123, 2003.

[11] B. M. Reid, R. Shastry, A. Gallimore, and R. Hofer, "Angularly-resolved E×B probe spectra in the plume of a 6-kW Hall thruster," in *Proc. 44th AIAA/ASME/SAE/ASEE Joint Propuls. Conf. Exhibit*, Hartford, CT, USA, Jul. 2008.

[12] M. L. R. Walker, "Effects of facility backpressure on the performance and plume of a Hall thruster," Ph.D. dissertation, Dept. Aerosp. Eng., Univ. Michigan, Ann Arbor, MI, USA, 2005.

[13] R. Hofer, D. Goebel, I. Mikellides, and I. Katz, "Design of a laboratory Hall thruster with magnetically shielded channel walls, phase II: Experiments," in *Proc. 8th AIAA/ASME/SAE/ASEE Joint Propuls. Conf. Exhibit*, Atlanta, GA, USA, Aug. 2012.

[14] M. J. Sekerak, "Plasma oscillations and operational modes in Hall effect thrusters," Ph.D. dissertation, Dept. Aerosp. Eng., Univ. Michigan, Ann Arbor, MI, USA, 2014.

[15] M. McDonald, C. Bellant, B. St Pierre, and A. Gallimore, "Measurement of cross-field electron current in a Hall thruster due to rotating spoke instabilities," in *Proc. 47th Joint Propuls. Conf.*, San Diego, CA, Aug. 2011.

[16] R. B. Lobbia, T. M. Liu, and A. D. Gallimore, "Correlating time-resolved optical and Langmuir probe measurements of Hall thruster dynamics," in *Proc. SPS*, Orlando, FL, USA, Dec. 2008.

[17] M. S. McDonald and A. D. Gallimore, "Rotating spoke instabilities in Hall thrusters," *IEEE Trans. Plasma Sci.*, vol. 39, no. 11, pp. 2952–2953, Nov. 2011.

[18] J. S. Bendat and A. G. Piersol, *Engineering Applications of Correlation and Spectral Analysis*. New York, NY, USA: Wiley, 1980.

[19] M. S. McDonald, "Electron transport in Hall thrusters," Ph.D. dissertation, Dept. Aerosp. Eng., Univ. Michigan, Ann Arbor, MI, USA, 2012.

[20] M. Sekerak, M. McDonald, R. Hofer, and A. Gallimore, "Hall thruster plume measurements from high-speed dual Langmuir probes with ion saturation reference," in *Proc. IEEE Aerosp. Conf.*, Big Sky, MT, USA, Mar. 2013, pp. 1–16.

[21] M. S. McDonald and A. D. Gallimore, "Comparison of breathing and spoke mode strength in the H6 Hall thruster using high speed imaging," in *Proc. IEPC*, Washington, DC, USA, Oct. 2013.

[22] F. S. Acton, *Analysis of Straight-Line Data*. New York, NY, USA: Wiley, 1959.

[23] P. Bevington and D. K. Robinson, *Data Reduction and Error Analysis for the Physical Sciences*. New York, NY, USA: McGraw-Hill, 1992.

[24] B. M. Reid, "The influence of neutral flow rate in the operation of Hall thrusters," Ph.D. dissertation, Dept. Aerosp. Eng., Univ. Michigan, Ann Arbor, MI, USA, 2009.

[25] R. Hofer *et al.*, "Efficacy of electron mobility models in hybrid-PIC Hall thruster simulations," in *Proc. 44th AIAA/ASME/SAE/ASEE Joint Propuls. Conf. Exhibit*, Hartford, CT, USA, Jul. 2008.

[26] T. H. Stix, *Waves in Plasmas*. New York, NY, USA: AIP, 1992.

[27] F. F. Chen, *Introduction to Plasma Physics and Controlled Fusion*. New York, NY, USA: Plenum, 1990.

[28] D. Escobar and E. Ahedo, "Ionization-induced azimuthal oscillation in Hall effect thrusters," in *Proc. IEPC*, Wiesbaden, Germany, Sep. 2011, pp. 1–13.

[29] J. Cavalier, N. Lemoine, G. Bonhomme, S. Tsikata, C. Honoré, and D. Grésillon, "Hall thruster plasma fluctuations identified as the E×B electron drift instability: Modeling and fitting on experimental data," *Phys. Plasmas*, vol. 20, no. 8, p. 082107, 2013.

[30] B. A. Jorns and R. R. Hofer, "Plasma oscillations in a 6-kW magnetically shielded Hall thruster," *Phys. Plasmas*, vol. 21, no. 5, p. 053512, May 2014.

Michael J. Sekerak received the B.S. (Hons.) degree in mechanical engineering from the Illinois Institute of Technology, Chicago, IL, USA, in 1999, the M.S. degree in aeronautics and the Engineer's degree in spacecraft and mission design from the California Institute of Technology, Pasadena, CA, USA, in 2001 and 2005, respectively, and the Ph.D. degree from the University of Michigan, Ann Arbor, MI, USA, in 2014, with a focus on high-speed plasma transients and oscillatory modes in Hall effect thrusters (HETs).

He conducted research on vacuum arc thrusters at the NASA Jet Propulsion Laboratory (JPL), Pasadena. He was called to active duty in the U.S. Army, and served five years as a Cavalry Officer, including one combat tour in Iraq and the Missile Correlation Center at the Cheyenne Mountain Air Force Station, Colorado Springs, CO, USA. From 2007 to 2010, he was an Aerospace and Propulsion Engineer with the Missile Systems Group, Sandia National Laboratories, Albuquerque, NM, USA, where he designed and launched vehicles in support of the Missile Defense Agency and the U.S. Navy. He is a Major with the Air Force Reserves, has taught science and spacecraft design lessons with the Reserve National Security Space Institute, and was involved in HETs with the Air Force Research Laboratory, Edwards AFB, CA, USA. He is currently a Systems Engineer with NASA JPL, where he is involved in researching electric propulsion and conducting mission formulation studies.

Benjamin W. Longmier received the Ph.D. degree in engineering physics from the University of Wisconsin-Madison, Madison, WI, USA, in 2007.

He served as the Principal Research Scientist with Ad Astra Rocket Company, Webster, TX, USA, where he was responsible for developing experiment campaigns and new plasma diagnostics appropriate for high-power engine and exhaust plume testing. He has served as a Principal Investigator and Project Manager for six NASA microgravity spacecraft technology development programs over the past eight years with six cumulative hours in microgravity. He completed a postdoctoral fellowship with the National Aeronautics and Space Administration, Greenbelt, MD, USA, and the University of Houston, Houston, TX, USA. In 2011, he was appointed as the Chair of the new American Institute for Aeronautics and Astronautics National Educator Academy-High Altitude Balloon Program to enhance student aerospace education nationwide. He is currently an Assistant Professor with the Department of Aerospace Engineering, University of Michigan, Ann Arbor, MI, USA. He is developing the next generation of advanced thrusters from 10 W to 200 kW to enable wide access to remote destinations within the solar system. His current research interests include electric propulsion, spacecraft and aerostat design, low-temperature plasma physics, plasma materials interaction, and plasma diagnostics.

Alec D. Gallimore received the B.S. degree in aeronautical engineering from the Rensselaer Polytechnic Institute, Troy, NY, USA, and the M.A. and Ph.D. degrees in aerospace engineering from Princeton University, Princeton, NJ, USA, with a focus on plasma physics.

He is currently an Arthur F. Thurnau Professor of Aerospace Engineering with the University of Michigan, Ann Arbor, MI, USA, where he directs the Plasmadynamics and Electric Propulsion Laboratory. He has supervised 36 Ph.D. students and 12 master's students, and has authored over 300 journal articles and conference papers on electric propulsion and plasma physics. His current research interests include advanced spacecraft propulsion, plasma physics, and nanoparticle energetics.

Daniel L. Brown received the B.S.E. degree in aeronautics and astronautics from the University of Washington, Seattle, WA, USA, in 2003, and the M.S.E. and Ph.D. degrees in aerospace engineering from the University of Michigan, Ann Arbor, MI, USA, in 2005 and 2009, respectively.

He currently leads advanced electric propulsion research and development with the Air Force Research Laboratory, Edwards AFB, CA, USA. He is an expert in Hall thruster technology and leads efforts spanning from fundamental research to the support of flight programs with the Department of Defense. He currently manages research of next-generation electric propulsion concepts and guides Air Force investments in academia and industry. He has authored over 34 journal articles and conference papers in the field of electric propulsion.

Dr. Brown is the Chair of the Joint Army Navy NASA Air Force Spacecraft Propulsion Subcommittee and a member of the AIAA Electric Propulsion Technical Committee.

Richard R. Hofer received the B.S.E. degree in mechanical engineering, and the B.S.E., M.S.E, and Ph.D. degrees in aerospace engineering from the University of Michigan, Ann Arbor, MI, USA, in 1998, 1998, 2000, and 2004, respectively.

He is currently a Senior Engineer with the Jet Propulsion Laboratory (JPL), Pasadena, CA, USA, where he is also the Technology Lead responsible for the development and qualification of Hall thrusters for deep space missions. He is a recognized expert in Hall thruster design, having designed several advanced Hall thrusters ranging in power from 1 to 100 kW. Thruster technology developed by him is currently used in every internal Hall thruster development of the U.S. Government. He has authored over 90 technical publications in the field of electric propulsion.

Dr. Hofer is an Associate Fellow of the American Institute of Aeronautics and Astronautics (AIAA) and a member of the AIAA Electric Propulsion Technical Committee. He was a recipient of the NASA Exceptional Achievement Medal and the JPL Lew Allen Award for Excellence, in 2011.

James E. Polk received the B.S. degree in aerospace engineering from the Georgia Institute of Technology, Atlanta, GA, USA, and the Ph.D. degree in mechanical and aerospace engineering from Princeton University, Princeton, NJ, USA.

He was the Task Manager for a successful 8200 h wear test of a 2.3-kW ion engine and supported the ion propulsion technology validation activities on the New Millennium Deep Space 1 flight project. He was a co-investigator of the NASA's Next Generation Ion Propulsion Program and the Advanced Lithium-Fed Applied-Field Lorentz Force Accelerator Program, and the Principal Investigator of the Nuclear Electric Xenon Ion System Program, which was focused on the development of a high-power high-specific impulse ion thruster. He managed the Venus Extreme Environments Strategic Initiative, which developed technologies for Venus lander missions. From 1997 to 2001, he served as the Supervisor of the Advanced Propulsion Group at the Jet Propulsion Laboratory (JPL), Pasadena, CA, USA. He is currently a Principal Engineer with the Propulsion and Materials Engineering Section, JPL, where he has been for the last 21 years. He is also a Lecturer with Graduate Aerospace Laboratories, California Institute of Technology, Pasadena, where he teaches a graduate-level space propulsion class. He is currently managing the JPL's high-power electric propulsion tasks as part of the In-Space Propulsion Project under the Space Technology Mission Directorate. He is an expert in the area of high-current cathode physics, ion engine wear processes, high-power plasma thrusters, and the application of probabilistic methods to analysis of engine service life, and has considerable experience in the development of Arcjet thrusters and Hall thrusters. He has authored over 100 papers in the field of electric propulsion.

Dr. Polk has received five best paper awards at the International Electric Propulsion Conference and the Joint Propulsion Conference.